Mechanism of photoexcited precession of magnetization in (Ga,Mn)As on the basis of time-resolved spectroscopy

T. Matsuda* and H. Munekata

Imaging Science and Engineering Laboratory, Tokyo Institute of Technology, 4259-J3-15 Nagatsuta, Midori-ku, Yokohama 226-8503, Japan

(Received 29 August 2014; revised manuscript received 19 January 2016; published 12 February 2016)

In order to investigate the mechanism of photoexcited precession of magnetization in ferromagnetic $Ga_{1-x}Mn_xAs$, magneto-optical (MO) and differential reflectivity ($\Delta R/R$; DR) temporal profiles are studied at relatively long (picosecond to nanosecond) and ultrashort (1 ps or less) time scales for samples with different Mn content ($x = 0.01-0.11$). As to the oscillatory MO profiles observed in the long time scale, simulation based on the Landau-Lifshitz-Gilbert equation combined with two different MO effects confirms photoinducement of the perpendicular anisotropy component $\Delta H_{\mathrm{eff},\perp}$. As for the profiles observed in the ultrashort time scale, they are consistently explained in terms of the dynamics of photogenerated carriers, but not by the sudden reduction in magnetization (the ultrafast demagnetization). In light of these experimental results and analyses, a mechanism that accounts for the photoinduced $\Delta H_{\mathrm{eff},\perp}$ is addressed: namely, photoionizationlike excitation of Mn^{2+}, $Mn^{2+} + h\nu \rightarrow Mn^{2+,*} = Mn^{3+} + e^-$. That such excitation tips magnetic anisotropy toward the out-of-plane direction through the inducement of orbital angular momentum and the gradient $\partial(Mn^{2+,*})/\partial z$ is discussed. The validity of the proposed mechanism is examined by estimating the efficiency of excitation on the basis of the Lambert-Beer law and the experimental $\Delta H_{\mathrm{eff},\perp}$ values, through which an efficiency of 1–10 ppm with a nominal optical cross section of around 5×10^{-12} m^2 is obtained.

DOI: 10.1103/PhysRevB.93.075202

I. INTRODUCTION

The present work focuses on photoexcited precession of magnetization (PEPM) in the *p*-type, ferromagnetic semiconductor (Ga,Mn)As [1–10]. It has been established that PEPM in *p*-(Ga,Mn)As is triggered by femtosecond (fs) laser pulses of photon energy near the GaAs band gap with relatively low laser fluence ($0.1-10\,\mu J/cm^2$), without external fields or angular momentum of light. This fact indicates that the weak excitation itself tips the effective field $\boldsymbol{H}_{\mathrm{eff}}$ away from equilibrium and exerts torque on magnetization $\boldsymbol{M}$, which contrasts greatly with PEPM in metals and insulators [11,12].

Researchers have inferred that direction of the $\boldsymbol{H}_{\mathrm{eff}}$ vector varies in the plane as the consequence of imbalance between bulk-cubic and interface-uniaxial anisotropies due to an ultrafast rise in either hole concentration or temperature of the spin subsystem [2–4,7–9]. This scenario, however, has been challenged in work that analyzes both oscillatory and dc components of PEPM with simulations based on the Landau-Lifshitz-Gilbert equation combined with two different magneto-optical (MO) effects; namely polar Kerr rotation I_z and magnetic birefringence I_{xy} [13,14] (the LLG-2MO simulation, Fig. 1). The $\boldsymbol{H}_{\mathrm{eff}}(t)$ vector, whose blunt dynamic response differs from the abrupt optical response induced by photogenerated carriers [15], is found to be tipped toward the out-of-plane direction [5,6]. While the photoinduced perpendicular anisotropy component, $\Delta H_{\mathrm{eff},\perp}$, has been confirmed by others [9], the $\Delta H_{\mathrm{eff},\perp}$ mechanism needs to be explained by a model beyond the *p-d* Zener model [16,17], which only assumes an interaction between Mn^{2+} ions and free holes.

Motivated by the foregoing background, optical responses of various $Ga_{1-x}Mn_xAs$ samples with different Mn content x have been investigated at two different time scales: the relatively long time scale at which precession of magnetization takes place (picosecond to nanosecond) and the so-called ultrashort time scale (1 ps or less) at which a precursory process that triggers PEPM may be optically detected. Temporal MO profiles in the long time scale have been successfully modeled by the LLG-2MO simulation by only introducing a photoinduced perpendicular component, $\Delta H_{\mathrm{eff},\perp}$. The simulation reveals that $\Delta H_{\mathrm{eff},\perp}$ is generated relatively faster (10–20 ps) for below-gap excitation than for above-gap excitation (~100 ps), suggesting that the pathway of energy transfer from electrons to spins is dependent on the band structure near the band edges. In the ultrashort timescale, rapidly oscillating signals have been observed for below-gap excitations, whereas spikelike signals have appeared for above-gap excitation (except for the $x = 0.01$ sample). The autocorrelation approach has been adopted to analyze those signals, which suggests that both types of signals reflect the dynamics of photogenerated carriers, but are not directly associated with spin or magnetization dynamics. Simulation with the Landau-Lifshitz-Bloch (LLB) equation including longitudinal relaxation of macrospins has failed to reproduce the experimental *positive* spikes in the sense that the LLB simulation always yields *negative* spikes as the consequence of ultrafast reduction of in-plane magnetization.

On the basis of these findings, we have concluded that ultrafast demagnetization is not the primary mechanism that triggers PEPM, and have addressed a mechanism for the photoinduced $\Delta H_{\mathrm{eff},\perp}$; namely, photoionizationlike excitation of Mn^{2+}, $Mn^{2+} + h\nu \rightarrow Mn^{2+,*} = Mn^{3+} + e^-$. Here, what brings about the anisotropy along the z axis is the orbital angular momentum of the Mn^{3+} component [18] together with the dynamic concentration gradient $\partial(Mn^{2+,*})/\partial z$. The efficiency of excitation has been estimated to be 1–10 ppm,

*Present address: Advanced Technology R&D Center, Mitsubishi Electric Corp., 8-1-1 Tsukaguchi-honmachi, Amagasaki City, Hyogo 661-8661, Japan.

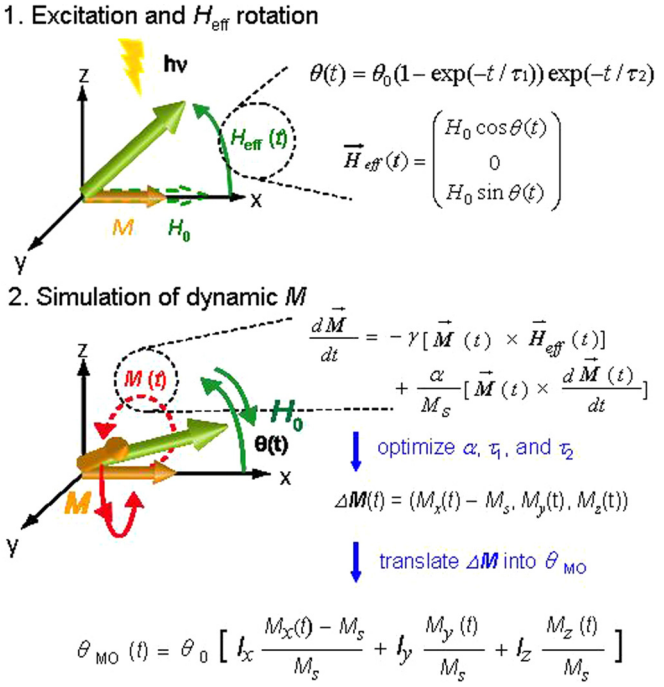

FIG. 1. Schematic illustration of steps in the LLG-2MO simulation. A laser pulse results in a change in the direction of an effective magnetic field $\boldsymbol{H}_{\rm eff}(t) = [H_0\cos\theta(t), 0, H_0\sin\theta(t)]$ with dynamic rotation function $\theta(t)$. A magnetization vector $\boldsymbol{M}(t)$ precesses around the $\boldsymbol{H}_{\rm eff}(t)$ with natural damping, and yields differential MO signals $\Theta_{\rm MO}(t)$, which is the linear combination of magnetic birefringence $I_x\Delta M_x$ and $I_y\Delta M_y$, and polar Kerr rotation $I_z\Delta M_z$. α and γ in the LLG equation are the effective Gilbert damping coefficient and gyromagnetic constant, respectively.

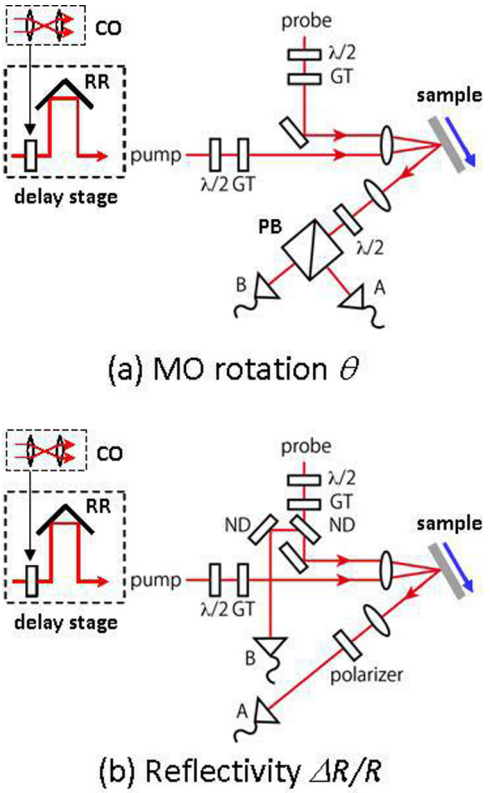

FIG. 2. Schematic illustrations of experimental setups for (a) MO and (b) DR measurements. Delay stages built upstream of the pump lines are also shown in the insets. RR, λ/2, GT, PB, ND, and CO represent, respectively, the retroreflector, half-wave plate, Glan-Thompson prism, polarizing beam splitter, neutral density filter, and collimator. CO consists of a pair of lenses. The optical bridge is composed of photodiode detectors A and B. MO rotation θ is obtained by $\theta = (A-B)/2B$, $A \approx B$, whereas differential reflectivity is obtained by $\Delta R/R = (A-B)/2B$. Arrows behind samples represent in-plane (x-y plane), remnant magnetization of samples. Photoinduced anisotropy occurs along the out-of-plane, z axis, as shown in Fig. 1.

together with a nominal optical cross section of around $5 \times 10^{-12}\,\mathrm{m}^2$. The relatively large cross-section value could be regarded as a clue to quantifying the magnitude of p-d hybridization around the valence-band top, which has been discussed theoretically [19,20].

II. EXPERIMENT

Four 100-nm-thick $Ga_{1-x}Mn_xAs$ epilayers ($x = 0.01$, 0.02, 0.08, 0.11), grown on LT-GaAs/GaAs(001) substrates at 235 °C by molecular beam epitaxy, were studied. They show an in-plane magnetic easy axis nearly along the GaAs ⟨100⟩ axis at low temperatures (<20 K), and exhibit so-called metallic conduction at low temperatures [21]. Temporal profiles of magneto-optical (MO) and differential reflectivity ($\Delta R/R$; DR) signals were measured by using a one-color, pump-and-probe (P-P) system based on a mode-locked Ti:sapphire laser whose pulse duration and repetition rate were around 150 fs and 76 MHz, respectively. The wavelength of the laser was varied between 750 and 900 nm ($h\nu = 1.38-1.65$ eV). Experimental setups for the MO and DR measurements are shown schematically in Figs. 2(a) and 2(b), respectively.

As summarized schematically in Fig. 1, the LLG-2MO simulation handles both oscillatory and dc components of MO temporal profiles, and extracts dynamics of photoinduced $\boldsymbol{H}_{\rm eff}(t)$. For this reason, great care was taken to maintain a stable optical baseline extended up to 3 ns, as well as a high signal-to-noise ratio; the positions of a collimator and a retroreflector in an optical delay line were precisely adjusted so as to retain the same beam diameter at the point 10 m from the delay line throughout the entire range of the delay time (Fig. 2). Pump and probe beams, whose polarizations are both $\boldsymbol{E} \parallel$ GaAs[010], were focused into the same spot of around 100 μm diameter using a CCD camera equipped with a long-focus microscope. Precision of the overlap was 10–20 μm. The incident angles with respect to the axis normal were around 6° and 3° for the pump and probe beam, respectively. A reflected probe beam was guided into an optical bridge that was placed 1.8 m from the sample plane. The time interval of probing in the ultrafast time region ($t < 4$ ps) was 26 fs as determined by the precision of a mechanical delay stage. All P-P measurements were carried out at 10 K. Prior to the measurements, samples were magnetized by applying an external field of $B = 0.2$ T along the in-plane, [010] direction. No external fields were applied during the measurements.

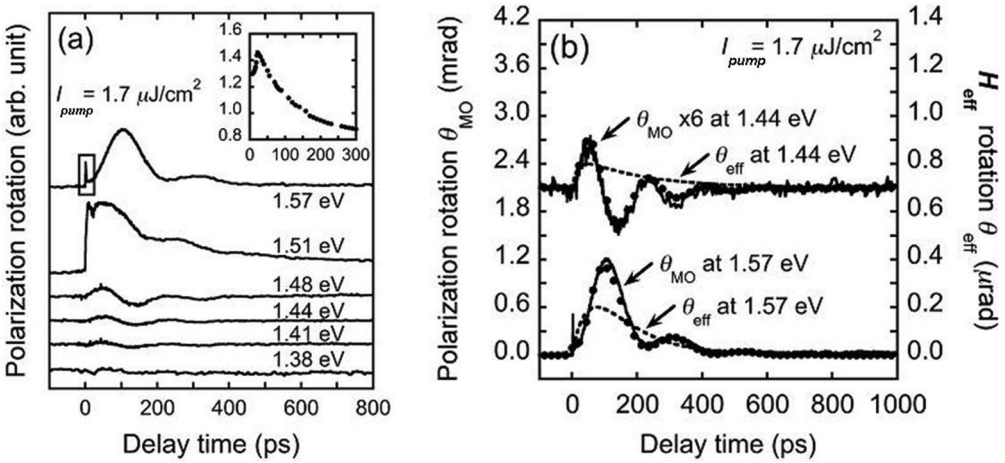

FIG. 3. (a) Temporal MO profiles obtained from the $x = 0.02$ sample with six different P-P photon energies. Pump fluence is fixed at $I_{pump} = 1.7\,\mu J/cm^2$. The inset shows temperature dependence of sample resistance; horizontal and vertical axes represent temperature (in K) and resistance (in kΩ), respectively. (b) Simulated MO profiles (dots) and experimental MO profiles (solid lines) for above- and below-gap excitation, together with profiles of the dynamic rotation function θ_{eff} (dashed lines).

III. RESULTS

Shown in Fig. 3(a) are long-time-scale temporal profiles of MO signals obtained for the $x = 0.02$ sample at six different P-P photon energies. No background subtraction was carried out from the raw MO data. A resistance-temperature curve of the $x = 0.02$ sample is depicted in the inset of Fig. 3(a). The fluence of pump and probe pulses was kept constant at $I_{pump} = 1.7\,\mu J/cm^2$ and $I_{probe} = 84\,nJ/cm^2$, respectively. In the MO profile taken at $h\nu = 1.57$ eV, note the presence of a spikelike component in the time domain of a few picoseconds, as highlighted by a rectangle, along with damping oscillation due to PEPM. This component always appears on the same side of the first peak of oscillations. At $h\nu = 1.51$ eV, being nearly the band-edge excitation, both the amplitude of the oscillation and the height of the spike are reduced. Simultaneously, the phase of the oscillatory component shifts toward a shorter time scale. A large, long-lived exponential component with a lifetime of around 2300 ps is presumed to be the carrier dynamics in a GaAs substrate [15,22]. Further decreasing P-P photon energy ($h\nu \leqslant 1.48$ eV) results in the disappearance of the spikelike component, whereas damping oscillation remains in the profiles down to $h\nu = 1.41$ eV ($\lambda = 880$ nm) without any further phase shift. The observed, gradual reduction in PEPM amplitude with decreasing photon energy suggests the excitation of the band-edge tails caused by Mn-related local potential fluctuations in (Ga,Mn)As [23].

Graphical representations of fitting experimental data with the LLG-2MO simulation are shown in Fig. 3(b). For both above- and below-gap excitations, the entire PEPM profile is well reproduced by the simulation, assuming the change in $\boldsymbol{H}_{eff}$ toward the z axis with the rotation function $\theta(t) = \theta_0\{1 - \exp(-t/\tau_1)\}\exp(-t/\tau_2)$, in which $(\tau_1,\tau_2) = (90,120)$ and (20,200) in picoseconds for the excitation at $h\nu = 1.57$ and 1.44 eV, respectively. Physical quantities associated with PEPM are summarized in Table I for different photon energies. The relatively small τ_1 value (fast rising $\Delta H_{eff,\perp}$) at the excitation at $h\nu = 1.4-1.5$ eV suggests that below-gap photons excite the states that couple more efficiently with ferromagnetically ordered spins. Study in the range $h\nu \geqslant 1.57$ eV reveals a slower rising $\Delta H_{eff,\perp}$ with increasing $h\nu$ values, which we discuss in a separate paper in connection with time-dependent MO coefficients induced by photogenerated free carriers [24,25].

Polarization dependences of pump-probe pulses on temporal MO profiles are shown in Fig. 4(a) for below-gap excitation. Similar to those obtained by above-gap excitation [5], inversion of the oscillation phase is clearly seen when polarization of the probe pulses is rotated 90°, between [010] and [100]. At the intermediate polarization of [110], oscillation is suppressed. The observed results indicate that precession of magnetization is detected primarily through the magnetic birefringence (MB) term I_{xy} [13,14]. A negligibly small contribution of the polar Kerr rotation (PKR) term I_z at $h\nu < 1.51$ eV is most likely due to multilayer interference [14] and the wavelength-dependent complex refractive index [26]. See Table I for the complicated x dependence on the ratio of MO coefficients. It is worth stressing that, if $\boldsymbol{M}$ starts precessing toward the out-of-plane direction (z axis),

TABLE I. Parameters of PEPM dynamics extracted by the LLG-2MO simulation using temporal MO profiles obtained from three samples with different Mn content. Rotation angle θ_0 of the $x = 0.02$ sample was determined by independently measured magneto-optical hysteresis data.

Mn content x	T_C (K)	$h\nu$ (eV)	$\boldsymbol{H}_{eff}$ (Oe)	α	θ_0 (μdeg)	τ_1 (ps)	τ_2 (ps)	I_z/I_{xy}
0.01	45	1.57	2600	0.27		80	2000	−10
		1.44	2800	0.40		10	450	−15
0.02	47	1.57	1800	0.25	38	90	120	+1.5
		1.48	2000	0.25	16	20	200	0.0
		1.44	2000	0.25	8	20	200	0.0
		1.41	2000	0.25	6	20	200	0.0
0.08	110	1.57	1055	0.06		90	1400	−2.7
		1.44	1055	0.08		90	1400	−3.1

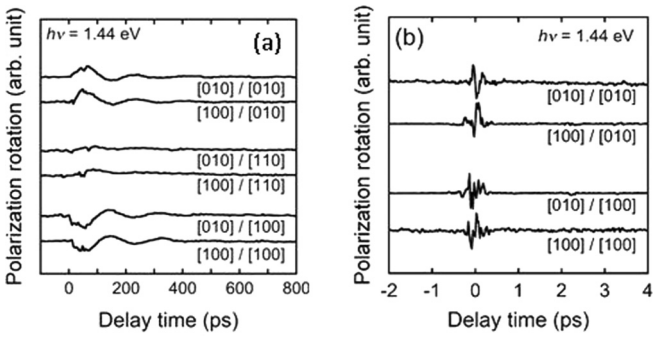

FIG. 4. Temporal MO profiles obtained with various combinations of pump and probe polarization for (a) long and (b) short time scales. P-P photon energy is $h\nu = 1.44\,\mathrm{eV}$. The label [xxx]/[xxx] below each profile specifies the polarization of pump and probe pulses, respectively; for instance, [100]/[010] represents a pump polarization of [100] and a probe polarization of [010]. All experimental data were obtained at pump and probe fluences of $I_{\mathrm{pump}} = 1.7\,\mu\mathrm{J/cm^2}$ and $I_{\mathrm{probe}} = 84\,\mathrm{nJ/cm^2}$, respectively.

the amplitude of oscillation would not be as large as in the experimental data [Fig. 4(a)] for the first tens of picoseconds due to the small I_z value. Moreover, the phase of oscillation would not change with polarization of probe pulses, if PKR is the primary MO effect that yields the observed MO signals.

We now focus on time scales of less than a few picoseconds. Figure 5(a) shows MO temporal profiles obtained at excitation energy $h\nu = 1.44\,\mathrm{eV}$ for various pump fluences I_{pump} ranging between 0.34 and $10\,\mu\mathrm{J/cm^2}$. We find rapidly oscillating signals around the time zero throughout the entire range of I_{pump}. The temporal DR profile also exhibits a similar type of oscillating signal [Fig. 5(b)], indicating that the observed rapid oscillation is attributed to the change in refractive index induced by photoexcited electronic polarization $\boldsymbol{P}$ [27].

Analysis of the rapid oscillation has been carried out on the basis of autocorrelation functions [28], which is represented by

$$\Delta r(t) = \Delta r^0 \int_{-\infty}^{t} f(t-\tau)|E_{\mathrm{pump}}(\tau) + E_{\mathrm{probe}}(\tau)|^2 d\tau, \quad \text{(1a)}$$

$$S^{(1)}(t) = \int_{-\infty}^{\infty} |\{r^0 + \Delta r(\tau')\}E_{\mathrm{probe}}(\tau')|^2 d\tau'. \quad \text{(1b)}$$

Equation (1a) represents the optical response at a sample surface $\Delta r(t)$ induced by electric fields of pump and probe pulses, $E_{\mathrm{pump}}(t) = E^0_{\mathrm{pump}}(t)\exp(-i\omega t)$ and $E_{\mathrm{probe}}(t) = E^0_{\mathrm{probe}}(t)\exp(-i\omega t)$, respectively, whereas Eq. (1b) represents the intensity of reflected probe light $S^{(1)}(t)$ affected by the coherent component of a reflected light pulse. Pulse envelopes are expressed by $I_{\mathrm{pump}}(t) = I^0_{\mathrm{pump}}G(t) = |E^0_{\mathrm{pump}}(t)|^2$ and $I_{\mathrm{probe}}(t - t_{\mathrm{delay}}) = I^0_{\mathrm{probe}}G(t - t_{\mathrm{delay}}) = |E^0_{\mathrm{probe}}(t - t_{\mathrm{delay}})|^2$, in which t_{delay} is the time delay of a probe pulse and $G(t)$ the Gaussian function. The calculated profile that reproduces the experimental data [Fig. 5(b)] is obtained with $\Delta r^0/r^0 = 0.01$ and the response function $f(t) = \exp(-t/40\,\mathrm{fs})$, together with the experimental conditions of $I^0_{\mathrm{pump}} = 1.7\,\mu\mathrm{J/cm^2}$ and $I^0_{\mathrm{probe}} = 84\,\mathrm{nJ/cm^2}$, and the standard deviation in $G(t)$, $\sigma = 38.6\,\mathrm{fs}$. The fast decoherence time constant $T = 40\,\mathrm{fs}$ in $f(t)$ cannot be attributed to spin-flip scattering since ferromagnetic order persists during the excitation. The presence of another mechanism was suggested in the studies of four-wave mixing (FWM) spectroscopy in CdMnTe under high magnetic fields [29] and (Ga,Mn)As with $x \leqslant 0.001$ [30], but was left open. We discuss this point later in relation to photoionizationlike excitation of Mn^{2+}.

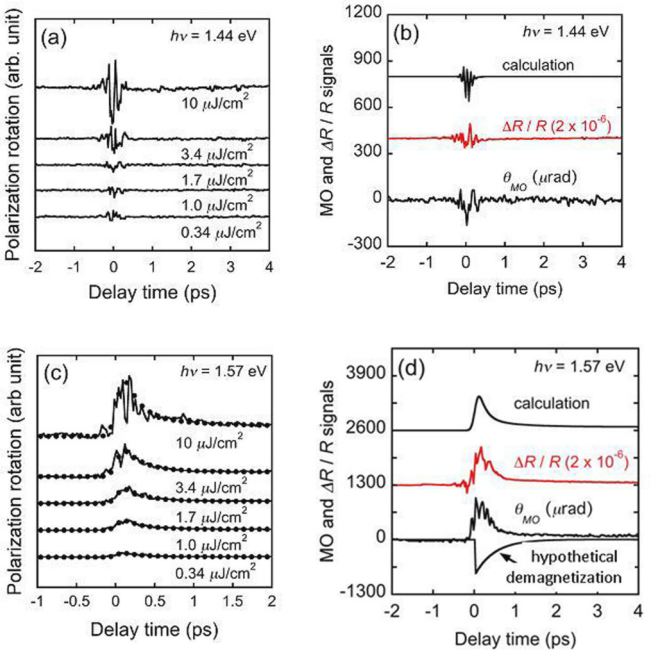

FIG. 5. (a) Temporal MO profiles obtained from the $x = 0.02$ sample by below-gap excitation with five different pump fluences. (b) Three different profiles, from the top, as follows: profile calculated using Eqs. (1a) and (1b), experimental differential reflectance profile, and experimental polarization rotation profile. Both experimental data were obtained at the pump fluence $I_{\mathrm{pump}} = 1.7\,\mu\mathrm{J/cm^2}$. (c) Temporal MO profiles obtained from the same sample by above-gap excitation with five different pump fluences, together with calculation using Eq. (2) (dots). (d) Four different profiles, from the top, as follows: calculation with autocorrelation function using Eq. (2), experimental differential reflectance profile, experimental polarization rotation profile, and calculated ultrafast demagnetization profile. Both experimental data were obtained at pump fluence $I_{\mathrm{pump}} = 1.7\,\mu\mathrm{J/cm^2}$. Profiles are intentionally shifted vertically for clarity.

Phase inversion by rotating the polarization of probe pulses 90° is not clearly established in rapidly oscillating MO signals [Fig. 4(b)]. The influence of pump-pulse polarization on oscillation phase is, rather, suggested in the signals. In considering of further searching for spin dynamics in the ultrashort time scale, it is interesting to examine experimental data with more precise simulation that takes into account ultrafast change in the polarization of E_{probe} caused by both carrier and spin dynamics. Further precise measurements, together with such advanced simulation, would shed light on the disturbance of ordered spins in the ultrafast time scale.

A rapidly oscillating component is replaced by a spike-like component for the above-gap excitation, as shown in Fig. 5(c). The spike-like component shown in Fig. 3(a) is thus reconfirmed by this measurement. Coexistence of the

oscillatory component is also noticeable at relatively high $I_{\rm pump}$. A DR temporal profile also shows mixing of these two components [Fig. 5(d)], which indicates that the observed spike is again attributed to the change in refractive index, but is now accompanied by the process which destroys, in part, the phase coherence between $E_{\rm pump}(t)$ and $E_{\rm probe}(t)$, namely by the thermalization of photogenerated free carriers [27]. With this inference in mind, Eq. (1b) is modified into Eq. (2) by omitting the interference terms $E^*_{\rm pump}E_{\rm probe}$ and $E_{\rm pump}E^*_{\rm probe}$:

$$S^{(2)}(t) = \int_{-\infty}^{\infty} \{r^0 + \Delta r(\tau')\} I_{\rm probe}(\tau') d\tau'. \qquad (2)$$

Calculated profiles using Eq. (2) are shown by solid symbols in Fig. 5(c) and the topmost solid line in Fig. 5(d). Through the calculations, we find that a response function consisting of the sum of two exponential decay components, $f(t) = \exp(-t/180\,{\rm fs}) + 0.12\ \exp(-t/900\,{\rm fs})$, reproduces the experimental data. Referring to the values of the time constants obtained by the calculation, we infer that the first exponential term ($T = 180$ fs) is associated with longitudinal optic (LO)-phonon scattering [31,32], whereas the second term ($T = 900$ fs) is associated with carrier trapping [33] or electron-hole-pair scattering by the background free holes [34]. While analysis using the incoherent part of autocorrelation stays at the level of phenomenological interpretations, it is clear that the spikelike feature appearing in case of above-gap excitation can be explained consistently in terms of thermalization of photogenerated carriers.

In order to further examine the effect of ultrafast heating caused by stronger optical absorption above the band-gap energy, calculation of MO profiles due to hypothetical demagnetization has been carried out using the Landau-Lifshitz-Bloch (LLB) equation [35]:

$$\frac{\partial \boldsymbol{M}}{\partial t} = \gamma \boldsymbol{M} \times \boldsymbol{H} + \gamma M_s \frac{\alpha_\perp}{M^2} \boldsymbol{M} \times (\boldsymbol{M} \times \boldsymbol{H}) - \gamma M_s \frac{\alpha_\parallel}{M^2} (\boldsymbol{M} \times \boldsymbol{H}) \boldsymbol{M}. \qquad (3)$$

Here, γ is the gyromagnetic constant, M_s saturation magnetization, and $\boldsymbol{H}$ the effective magnetic field, whereas $a_\perp \sim 0.25$ (see Table I) and $\alpha_\parallel$ are dimensionless transverse and longitudinal damping factors, respectively. Ultrafast demagnetization is expressed by the exponential function $\alpha_\parallel(t) = \alpha^0_\parallel \exp(-t/\tau_{\rm dem})$ with its magnitude $\alpha^0_\parallel = 0.09$ and 0.15 for $h\nu = 1.44$ and 1.57 eV, respectively. The lifetime $\tau_{\rm dem} \sim 0.4$ ps is chosen in view of reproducing the experimental data. $\boldsymbol{H}$ is assumed as $\boldsymbol{H} = \boldsymbol{H}_0 + \boldsymbol{H}_{\rm ext} + \boldsymbol{H}_{\rm dem}$, in which the in-plane crystal anisotropy field $|\boldsymbol{H}_0| \sim 2000$ Oe, an external field $|\boldsymbol{H}_{\rm ext}| = 0$, and the demagnetizing field $|\boldsymbol{H}_{\rm dem}| = 0$.

A *negative* spikelike component is obtained, reflecting the reduction of in-plane magnetization (M_x). In detail, our calculation yields a polarization rotation of 3.7 and 1.4 μrad, for $h\nu = 1.57$ and 1.44 eV, as shown by open circles in Figs. 6(a) and 6(b). These values correspond to a reduction in magnetization of 0.19% [Fig. 5(d)] and 0.13%, respectively, referring to the value of MO rotation measured separately in the process of 90° magnetization switching (Table I). Consequently, we find that the LLB simulation

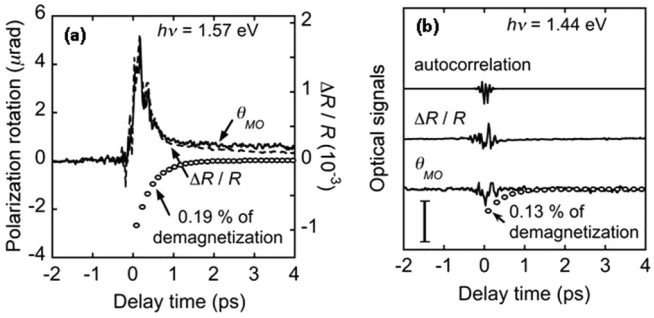

FIG. 6. Two examples of calculated temporal MO profiles due to hypothetical, ultrafast demagnetization using Eq. (3). (a) MO profile (open circles) plotted together with the spikelike component obtained by measurements with P-P photon energy $h\nu = 1.57$ eV, and (b) MO profile (open circles) plotted together with the rapidly oscillating component obtained by measurements with P-P photon energy $h\nu = 1.44$ eV. The length of the vertical bar in (b) represents a polarization rotation of 2 μrad. For all experimental data, $I_{\rm pump} = 1.7\,{\rm mJ/cm^2}$ and $I_{\rm probe} = 84\,{\rm nJ/cm^2}$.

always yields a *negative* spike, which is opposite that of the observed spikes. Therefore, we infer that the observed spike-like component is primarily attributed to the dynamics of photogenerated carriers. Otherwise, signals due to the ultrafast demagnetization are small, so that they are masked by the signals due to photogenerated carriers.

Interesting sample dependence is observed in the ultrashort time scale [Fig. 7(a)]. The rapidly oscillating component dominates for both below-and above-gap excitations in the $x = 0.01$ sample, which is near the boundary between insulator and metallic conditions [21]. On the other hand, spikelike components are conspicuous in the $x = 0.1$ sample, which is strongly metallic.

The MO profiles in the long time scale obtained by below-gap excitation [Fig. 7(b)] show that precession frequency

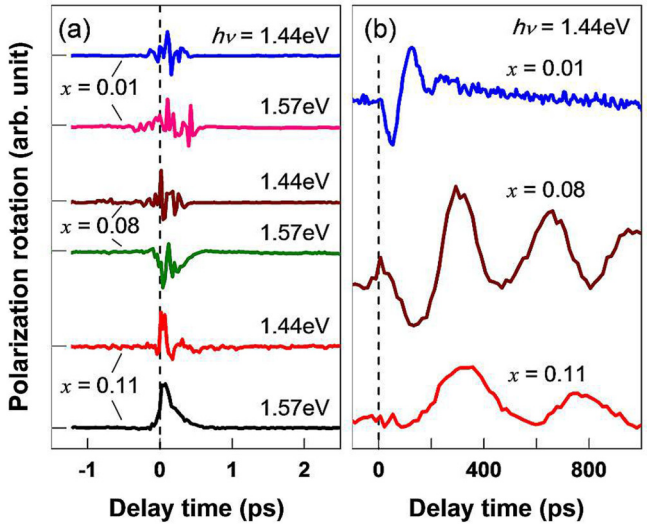

FIG. 7. (a) MO profiles obtained from $x = 0.01$, 0.08, and 0.11 samples with below- and above-gap excitations in (a) picosecond and (b) nanosecond time scales. Pump and probe fluences are $I_{\rm pump} = 1.7\,\mu{\rm J/cm^2}$ and $I_{\rm probe} = 84\,{\rm nJ/cm^2}$, respectively.

decreases with increasing x value, whereas damping tends to be minimized at intermediate x values. The observed trends are qualitatively similar to those obtained by above-gap excitation [36]. Analytical results obtained by the LLG-2MO simulation are compiled in Table I. We find that PEPM dynamics becomes less dependent on P-P photon energy for the $x = 0.08$ sample.

The τ_1 value, which represents the generation rate of $\Delta H_{\mathrm{eff},\perp}$, is nearly constant at the P-P photon energy of $h\nu = 1.57$ eV for all three samples, whereas it becomes shorter when excited at $h\nu = 1.44$ eV, particularly for the $x = 0.01$ and 0.02 samples. On the other hand, the τ_2 value, being the relaxation rate of $\Delta H_{\mathrm{eff},\perp}$, is obviously larger than the τ_1 value and tends to scatter among different samples, suggesting that the relaxation process is significantly influenced by extrinsic sources such as defects in the bulk and surfaces.

IV. DISCUSSION

In (Ga,Mn)As, it is experimentally established that the upper part in the valence band is strongly hybridized with the Mn d orbital [37–39], as shown schematically in Fig. 8. This gives rise to the notion that the interband excitation involves two different transitions; namely, hole-electron pair generation and photoionizationlike transition, $\mathrm{Mn}^{2+} + h\nu \rightarrow \mathrm{Mn}^{3+} + e^-$. The change in magnetization caused by the latter transition can be expressed by $\delta M^* = M^*(\mathrm{light}) - M(\mathrm{dark}) = \Delta\mathrm{Mn}^{2+,*}[p_m(\mathrm{Mn}^{3+}) - p_m(\mathrm{Mn}^{2+})]$. Here, $\Delta\mathrm{Mn}^{2+,*}$ is the number of excited Mn^{2+} ions (m^{-3}) in the unit sheet of (Ga,Mn)As with a thickness of one lattice constant ($a_0 = 0.565$ nm), whereas $p_m(\mathrm{Mn}^{3+})$ and $p_m(\mathrm{Mn}^{2+})$ are the magnetic moments of Mn^{3+} and Mn^{2+}, respectively. Assuming the g factor $g = 2.7$ [18] and the net spin number $S = 4/2$ for Mn^{3+}, and $g = 2.0$ and $S = 5/2$ for Mn^{2+}, we obtain $\delta M^* = 0.4\mu_B\gamma\hbar\Delta\mathrm{Mn}^{2+,*} = 4.68 \times 10^{-30}\,\Delta\mathrm{Mn}^{2+,*}$ with units of N/A m or Wb m^{-2}. Here, μ_B, γ, and $\hbar$ are the Bohr magneton, gyromagnetic ratio ($e/2m$), and Planck's constant, respectively. The increment in ΔM^* is attributed to the large g factor of Mn^{3+}, the orbital angular momentum. That is, ΔM^* can conceptually be regarded as the magnetization generated by a virtual current (a flow of kinetic energy) passing through a virtual solenoid (orbital) whose central axis is parallel to the z axis. Naturally, one of the most likely sources that yields such a current is the electrochemical potential gradient $\partial\mathrm{Mn}^{2+,*}/\partial z$ (Fig. 8 inset).

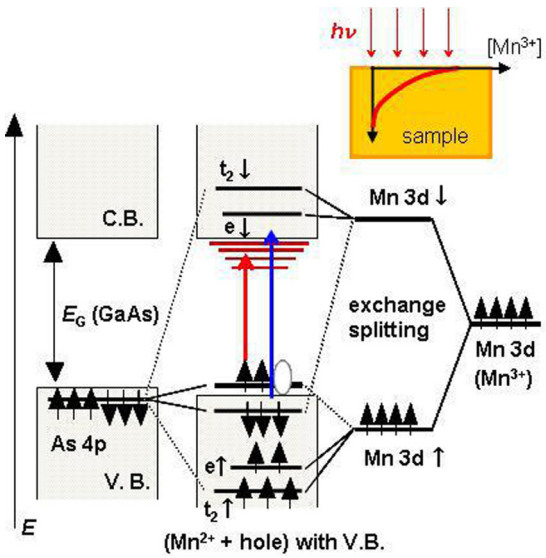

FIG. 8. Schematic illustration of electronic structure of (Ga,Mn)As resulting from p-d hybridization between As 4p states in the GaAs valence band (VB) and Mn 3d states in Mn^{2+} ions substituting for Ga sites. Joint Urbach tails are represented by brown horizontal lines below the edge of the conduction band (CB). Below- and above-gap excitations are represented by a short red and a long blue arrows, respectively. Inset, upper right, depicts excitation-induced spatial gradient of photoexcited $\mathrm{Mn}^{2+}(\mathrm{Mn}^{2+,*})$ ions.

Since the photoinduced effective field per sheet is expressed by $\delta H_{\mathrm{eff},\perp} = \delta M^*/\mu_0 = 3.71 \times 10^{-24} \times \Delta\mathrm{Mn}^{2+,*}$ [A/m] with μ_0 the vacuum permeability, the overall field induced by the photoexcitation is obtained by integrating $\delta H_{\mathrm{eff},\perp}$ over the entire layer thickness d in units of the lattice constant a_0 ($d = 100$ [nm] $= 1.77 \times 10^{11}$ [a_0]). On the basis of Lambert-Beer law, the number of $\mathrm{Mn}^{2+,*}$ ions produced in the unit sheet at the depth z (in units of the lattice constant a_0) is expressed by $\Delta\mathrm{Mn}^{2+,*}(z) = \beta[\mathrm{Mn}^{2+}]\alpha I = \beta[\mathrm{Mn}^{2+}]\alpha I_0 \exp(-\alpha z)$, in which β, $[\mathrm{Mn}^{2+}]$, I_0, and α are *nominal* absorption cross section (m^2), the number of Mn^{2+} ions in the unit sheet (m^{-3}), photon flux (m^{-2}), and absorption coefficient in the unit of inverse lattice constant (a_0^{-1}), respectively. Combining all, we obtain Eqs. (4a) and (4b) for the overall photoinduced field $\Delta H_{\mathrm{eff},\perp}$ and the total number of photoexcited Mn^{2+} ions, $[\mathrm{Mn}^{2+,*}]$, respectively:

$$\begin{aligned}\Delta H_{\mathrm{eff},\perp} &= \int_0^d \delta H_{\mathrm{eff},\perp} dz \\ &= 3.71 \times 10^{-24} \int_0^d \beta\Delta\mathrm{Mn}^{2+,*} I_0 \exp(-\alpha z) dz \\ &= 9.30 \times 10^{-7}\beta I_0\{1 - \exp(-\alpha d)\}, \qquad (4a)\\ [\mathrm{Mn}^{+2,*}] &= 2.51 \times 10^{17}\beta I_0\{1 - \exp(-\alpha d)\}. \qquad (4b)\end{aligned}$$

The values $I_0\{1 - \exp(-\alpha d)\}$ on the right-hand side of Eqs. (4a) and (4b) are 7.35×10^{14} and 6.4×10^{15} photons/m^2, with $\alpha = 5.65 \times 10^{-5}$ [a_0^{-1}] ($= 10^3\ \mathrm{cm}^{-1}$), $I_0 = 7.4 \times 10^{16}$ photons/m^2, and $\alpha = 5.65 \times 10^{-4}$ [a_0^{-1}] ($= 10^4\ \mathrm{cm}^{-1}$), $I_0 = 6.8 \times 10^{16}$ photons/m^2 at $h\nu = 1.44$ and 1.57 eV, respectively. As to the left-hand side of Eq. (4a), the peak θ_{eff} values of the temporal θ_{eff} profiles are obtained from the dotted lines in Fig. 3(b), which are $\theta_{\mathrm{eff,peak}} = 0.020$ and 0.21 μrad for $h\nu = 1.44$ and 1.57 eV, respectively. Then, the maximum $\Delta H_{\mathrm{eff},\perp}$ values are estimated to be 4.0×10^{-5} and 3.8×10^{-4} Oe for $h\nu = 1.44$ and 1.57 eV, respectively, using the z component of the magnetization rotation function, $H_0 \sin\theta(t)$ (Fig. 1). We finally obtain $\beta = 4.7 \times 10^{-12}$ and $5.1 \times 10^{-12}\ \mathrm{m}^2$ for $h\nu = 1.44$ and 1.57 eV, respectively. Although it is not a rigorous comparison, these values are obviously larger than the optical cross-section standards of transition-metal and rare-earth ions in optical materials including zinc-blende semiconductors [40–42]. Hybridization between Mn d orbitals and host valence bands may be responsible for the large β values. The activation efficiencies $[\mathrm{Mn}^{2+,*}]/[\mathrm{Mn}^{2+}]$ are

estimated by using Eq. (4b), which yields 1.9×10^{-6} and 1.8×10^{-5} for $h\nu = 1.44$ and 1.57 eV, respectively.

The time lag (τ_1) between the time of excitation and the time $\Delta H_{\mathrm{eff},\perp}$ reaches a maximum suggests that the photoionizationlike transition would be a subordinate process that follows the hole-electron pair generation. It is inferred that this transition occurs when excitation energy is transferred by the annihilation of hole-electron pairs (Auger recombination) or by the scattering between hole-electron pairs and Mn^{2+} ions. A reduced τ_1 value with decreasing excitation photon energy suggests that valence-band states near the Fermi level can influence Mn spins relatively faster, which is in accordance with the picture of strong p-d hybridization near the valence-band top [19,20].

V. CONCLUSIONS

We have presented time-resolved magneto-optical (MO) and differential reflectivity ($\Delta R/R$; DR) measurements at relatively long (picosecond to nanosecond) and ultrashort (1 ps or less) time scales for $Ga_{1-x}Mn_xAs$ samples with different Mn content ($x = 0.01-0.11$). Inducement of a perpendicular effective field component $\Delta H_{\mathrm{eff},\perp}$ has been confirmed by the MO temporal profiles obtained at relatively long time scales for different excitation photon energies combined with various polarization combinations of probe pulses, and by the analysis of those profiles using the simulation based on the Landau-Lifshitz-Gilbert equation incorporating two different magneto-optical effects (the LLG-2MO simulation). It has also been found that $\Delta H_{\mathrm{eff},\perp}$ is generated relatively faster (10–20 ps) for below-gap excitation than for above-gap excitation (~100 ps), suggesting that electronic states near the valence-band top as well as those slightly inside the band gap couple efficiently with ferromagnetically ordered spins.

In the ultrashort time scale, rapidly oscillating and positive spikelike signals have been observed with below- and above-gap excitations, respectively. Those signals have been carefully analyzed by the autocorrelation approach, and have been concluded that they are most likely attributable to the dynamics of photogenerated carriers; otherwise, signals due to ultrafast demagnetization are small enough to be masked by the signals from those carriers. The fact that rapidly oscillating signals are not accompanied by the sudden, negative change in the baseline at the time of excitation—the fingerprint of ultrafast demagnetization—indicates that, at least in the case of below-gap excitation, ultrafast demagnetization is not a requirement for the photoinduced $\Delta H_{\mathrm{eff},\perp}$.

Motivated by all of these experimental data, a mechanism of photoinduced perpendicular effective field $\Delta H_{\mathrm{eff},\perp}$ has been addressed, namely, photoionizationlike excitation of Mn^{2+}, $Mn^{2+} + h\nu \rightarrow Mn^{2+,*} = Mn^{3+} + e^-$. Here, Mn^{3+} represents the spin configuration of $3d^4$ with $g = 2.7$, whereas e^- is an electron in the conduction band or its tail states. The fact that such excitation alters magnetic anisotropy toward the out-of-plane direction (z axis) through the inducement of orbital angular momentum and the gradient $\partial(Mn^{2+,*})/\partial z$ has been discussed. The validity of the proposed mechanism has been examined through the estimation of the nominal optical cross section β on the basis of the Lambert-Beer law and the peak values in the dynamic $\Delta H_{\mathrm{eff},\perp}(t)$ curves obtained by experiments. A β value of around 5×10^{-12} m^2 has been obtained, which reflects strong p-d hybridization around the valence-band top.

ACKNOWLEDGMENTS

We thank K. Nishibayashi and N. Nishizawa for their technical advice on optical experiments and samples, and acknowledge partial support from the Advanced Photon Science Alliance Project (APSA) commissioned by the Ministry of Education, Culture, Sports, Science and Technology (MEXT), and from a Grant-in-Aid for Scientific Research (No. 22226002) from the Japan Society for the Promotion of Science (JSPS).

[1] A. Oiwa, H. Takechi, and H. Munekata, J. Supercond. **18**, 9 (2005).
[2] H. Takechi, A. Oiwa, K. Nomura, T. Kondo, and H. Munekata, Phys. Status Solidi C **3**, 4267 (2006).
[3] D. M. Wang, Y. H. Ren, X. Liu, J. K. Furdyna, M. Grimsditch, and R. Merlin, Phys. Rev. B **75**, 233308 (2007).
[4] J. Qi, Y. Xu, N. H. Tolk, X. Liu, J. K. Frudyna, and I. E. Perakis, Appl. Phys. Lett. **91**, 112506 (2007).
[5] Y. Hashimoto, S. Kobayashi, and H. Munekata, Phys. Rev. Lett. **100**, 067202 (2008).
[6] Y. Hashimoto and H. Munekata, Appl. Phys. Lett. **93**, 202506 (2008).
[7] E. Rozkotova, P. Nemec, P. Horodyska, D. Sprinzl, F. Trojanek, P. Maly, V. Novak, K. Olejnik, M. Curt, and T. Jungwirth, Appl. Phys. Lett. **92**, 122507 (2008).
[8] J. Qi, Y. Xu, A. Steigerwald, X. Liu, J. K. Furdyna, I. E. Perakis, and N. H. Tolk, Phys. Rev. B **79**, 085304 (2009).
[9] N. Tesařová, P. Němec, E. Rozkotová, J. Šubrt, H. Reichlová, D. Butkovičová, F. Trojánek, P. Malý, V. Novák, and T. Jungwirth, Appl. Phys. Lett. **100**, 102403 (2012).
[10] P. Němec, E. Rozkotová, N. Tesařová, F. Trojánek, E. De Ranieri, K. Olejnik, J. Zemen, V. Novák, M. Cukr, P. Malý, and T. Jungwirth, Nat. Phys. **8**, 411 (2012).
[11] B. Koopmans, Laser-induced magnetization dynamics, in *Spin Dynamics in Confined Magnetic Structures II*, edited by B. Hillebrands and K. Ounadjela (Springer, Berlin, 2003), p. 253.
[12] A. Kirilyuk, A. V. Kimel, and Th. Rasing, Rev. Mod. Phys. **82**, 2731 (2010).
[13] When it was found in (Ga,Mn)As, it was ascribed to magnetic circular dichroism: A. V. Kimel, G. V. Astakhov, A. Kirilyuk, G. M. Schott, G. Karczewski, W. Ossau, G. Schmidt, L. W. Molenkamp, and Th. Rasing, Phys. Rev. Lett. **94**, 227203 (2005).
[14] Later, it was revisited and ascribed to magnetic birefringence: B. Al-Qadi, N. Nishizawa, K. Nishibayashi, M. Kaneko, and H. Munekata, Appl. Phys. Lett. **100**, 222410 (2012).

[15] S. Kim, E. Oh, J. U. Lee, D. S. Kim, S. Lee, and J. K. Furdyna, J. Korean Phys. Soc. **49**, 1611 (2006).
[16] T. Dietl, H. Ohno, and F. Matsukura, Phys. Rev. B **63**, 195205 (2001).
[17] T. Jungwirth, J. Sinova, J. Masek, J. Kucera, and A. H. MacDonald, Rev. Mod. Phys. **78**, 809 (2006).
[18] J. Schneider, U. Kaufmann, W. Wilkening, M. Baeumler, and F. Kohl, Phys. Rev. Lett. **59**, 240 (1987).
[19] J. Inoue, S. Nonoyama, and H. Itoh, Phys. Rev. Lett. **85**, 4610 (2000).
[20] J.-M. Tang and M. E. Flatté, Phys. Rev. Lett. **92**, 047201 (2004).
[21] F. Matsukura, H. Ohno, and T. Dietl, III-V Ferromagnetic Semiconductors, in *Handbook of Magnetic Materials*, edited by K. H. Buschov (Elsevier, New York, 2003), p. 14.
[22] G. W. 't Hooft, W. A. J. A. van der Poel, L. W. Molenkamp, and C. T. Foxon, Phys. Rev. B **35**, 8281(R) (1987).
[23] M. Yildirim, S. March, R. Mathew, A. Gamouras, X. Liu, M. Dobrowolska, J. K. Furdyna, and K. C. Hall, Phys. Rev. B **84**, 121202(R) (2011).
[24] T. Matsuda and H. Munekata, Springer Proc. Phys. **159**, 5 (2014).
[25] T. Matsuda, K. Nishibayashi, and H. Munekata: Proc. SPIE **9167**, 91670M (2014).
[26] K. S. Burch, J. Stephens, R. K. Kawakami, D. D. Awschalom, and D. N. Basov, Phys. Rev. B **70**, 205208 (2004).
[27] C. F. Klingshirn, *Semiconductor Optics* (Springer, Berlin, 1997), p. 340.
[28] M. V. Lebedeva, O. V. Misochkoa, T. Dekorsyb, and N. Georgiev, J. Exp. Theor. Phys. **100**, 272 (2005).
[29] S. T. Cundiff, R. Hellman, M. Koch, G. Mackh, A. Waag, G. Landwehr, W. H. Know, and E. O. Göbel, J. Opt. Soc. Am. B **13**, 1263 (1996).
[30] M. Yildirim, S. March, R. Mathew, A. Gamouras, X. Liu, M. Dobrowolska, J. K. Furdyna, and K. C. Hall, Appl. Phys. Lett. **101**, 062403 (2012).
[31] R. Tommasi, P. Langot, and F. Vallée, Appl. Phys. Lett. **66**, 1361 (1995).
[32] G. Segschneider, T. Dekorsy, H. Kurz, R. Hey, and K. Ploog, Appl. Phys. Lett. **71**, 2779 (1997).
[33] I. S. Gregory, C. M. Tey, A. G. Cullis, M. J. Evans, H. E. Beere, and I. Farrer, Phys. Rev. B **73**, 195201 (2006).
[34] A. Leitenstorfer, A. Lohner, K. Rick, P. Leisching, T. Elsaesser, T. Kuhn, F. Rossi, W. Stolz, and K. Ploog, Phys. Rev. B **49**, 16372 (1994).
[35] N. Kazantseva, D. Hinzke, R. W. Chantrell and U. Nowak, Europhys. Lett. **86**, 27006 (2009).
[36] S. Kobayashi, Y. Hashimoto, and H. Munekata, J. Appl. Phys. **105**, 07C519 (2009).
[37] J. Okabayashi, A. Kimura, T. Mizokawa, A. Fujimori, T. Hayashi, and M. Tanaka, Phys. Rev. B **59**, R2486 (1999).
[38] J. Okabayashi, A. Kimura, O. Rader, T. Mizokawa, A. Fujimori, T. Hayashi, and M. Tanaka, Phys. Rev. B **64**, 125304 (2001), and references therein.
[39] M. Kobayashi, I. Muneta, Y. Takeda, Y. Harada, A. Fujimori, J. Krempaský, T. Schmitt, S. Ohya, M. Tanaka, M. Oshima, and V. N. Strocov, Phys. Rev. B **89**, 205204 (2014).
[40] R. H. Page, K. I. Schaffers, L. D. DeLoach, G. D. Wilke, F. D. Patel, J. B. Tassano, Jr., S. A. Payne, W. F. Krupke, K. T. Chen, and A. Burger, IEEE J. Quantum Electro. **33**, 609 (1997).
[41] E. Bringuier, J. Appl. Phys. **70**, 4505 (1991).
[42] R. Moncorgé, Current Topics in Rare-earth Lasers, in *Spectroscopic Properties of Rare Earths in Optical Materials*, edited by G. Kiu and B. Jacquier (Springer, Berlin, 2005), p. 342.